

# Theory of Microphase Separation in Elastomers

Manu Mannattil,<sup>1,2,\*</sup> Haim Diamant,<sup>1</sup> and David Andelman<sup>2</sup>

<sup>1</sup>*School of Chemistry, Tel Aviv University, Ramat Aviv, Tel Aviv 69978, Israel*

<sup>2</sup>*School of Physics and Astronomy, Tel Aviv University, Ramat Aviv, Tel Aviv 69978, Israel*

Inspired by recent experiments, we present a phase-field model of microphase separation in an elastomer swollen with a solvent. The imbalance between the molecular scale of demixing and the mesoscopic scale beyond which elasticity operates produces effective long-range interactions, forming stable finite-sized domains. Our predictions concerning the dependence of the domain size and transition temperature on the stiffness of the elastomer are in good agreement with the experiments. Analytical phase diagrams, aided by numerical findings, capture the richness of the microphase morphologies, paving the way to create stable, patterned elastomers for various applications.

*Introduction.*— The interplay between elasticity and phase separation has been widely explored in various contexts since Cahn’s classic work from the 1960s on spinodal decomposition [1]. For example, a mismatch in the constituents’ elastic moduli in metallic alloys can either hinder or speed up phase separation [2]. Similarly, elasticity regulates the morphology of the phase-separated domains in gels [3–5] and liquid-crystalline fluids [6], which can lead to intricate patterns. Besides, mounting evidence now indicates that phase separation and elasticity are both crucial to the development of many membrane-less organelles within biological cells, rekindling interest in the topic [7–11]. To sidestep the complexities of the biological world, several experiments have been conducted with synthetic, *in vitro* model systems in the past few years [12–16]. The results of these experiments, along with related theoretical work [17–23], once again emphasize the influence of elasticity on phase separation in soft matter systems.

A recent experiment showed elasticity-controlled microphase separation to be a highly effective technique for generating patterned elastomers with complex morphologies [24]. In the experiment, a temperature quench triggers microphase separation in swollen elastomers. Elasticity was observed to arrest phase separation, resulting in a stable bicontinuous microstructure or droplets with a characteristic size of a few microns. This microphase separation plausibly arises because of a pronounced difference in the length scales at which thermodynamics and elasticity operate. This is unlike previous examples, where patterned phases were primarily seen in systems with anisotropic elasticity or external stresses [25] or involving nontrivial phenomena such as cavitation [18, 26].

In this Letter, we introduce a minimal phase-field model that captures the key features of microphase separation in swollen elastomers in the limit of weak segregation. We show that it is possible to address the length-scale discrepancy between elasticity and thermodynamics by employing a continuous order parameter and coarse-graining it further. The resulting long-range interactions lead to the emergence of stable, finite-sized domains whose length scale is governed by the stiffness of the elastomer.

Our scaling results for the domain size and microphase separation temperature agree with experimental observations. We also highlight the diversity of the microphase morphologies by constructing a phase diagram and supplementing it with numerical results. Put together, our findings underscore an intricate coupling between thermodynamics and elasticity, opening up novel ways to produce patternable materials for various purposes.

*Model.*— We consider a charge-neutral elastomer consisting of a cross-linked polymer network isotropically swollen with a solvent. Polymer-solvent interaction occurs over typical intermolecular distances (e.g., the size of the solvent molecules). On the other hand, the elastic response of the elastomer stems entirely from the underlying polymer network, which has a much larger, usually mesoscopic, characteristic length scale (Fig. 1). Deformations of the elastomer occurring below this length scale should not engender a significant elastic response. Elastomers can undergo large deformations during swelling, and they are customarily studied using nonlinear elasticity [27]. However, once the elastomer is completely swollen, further elastic deformations are well described using linear elasticity in terms of a three-dimensional (3D) displacement field  $\mathbf{u}(\mathbf{x})$  defined over points  $\mathbf{x}$  on the elastomer [28]. The resulting strain field is  $\varepsilon = \frac{1}{2}[\nabla\mathbf{u} + (\nabla\mathbf{u})^T]$ , with  $(\nabla\mathbf{u})^T$  being the transpose of  $\nabla\mathbf{u}$ .

For a precise description of thermodynamic interactions caused by compositional changes in the elastomer,

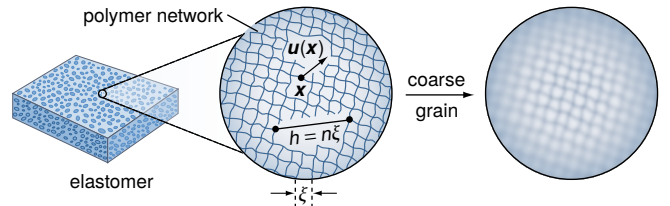


FIG. 1. Displacements  $\mathbf{u}(\mathbf{x})$  occurring below a characteristic length scale  $h$  do not stress the elastomer significantly. Using a coarse-grained strain field  $\bar{\varepsilon}$ , such displacements are “blurred away” and filtered out. In our model, we choose  $h$  as a multiple  $n\xi$  of the end-to-end distance  $\xi$  between adjacent cross-links of the polymeric network within the elastomer.

\* manu.mannattil@posteo.net

the continuum fields  $\mathbf{u}$  and  $\boldsymbol{\varepsilon}$  must both be defined at molecular length scales. However, only those deformations occurring above a much larger length scale stress the elastomer substantially. To address this, we consider a constitutive stress-strain relationship of the form

$$\boldsymbol{\sigma}(\boldsymbol{\varepsilon}) = \lambda(\text{tr } \bar{\boldsymbol{\varepsilon}}) \mathbb{1} + 2\mu \bar{\boldsymbol{\varepsilon}}, \quad (1)$$

where  $\lambda$  and  $\mu$  are the Lamé parameters,  $\mathbb{1}$  is the  $3 \times 3$  identity matrix, and  $\text{tr } \bar{\boldsymbol{\varepsilon}}$  denotes the trace of a coarse-grained strain  $\bar{\boldsymbol{\varepsilon}}$ , defined by

$$\bar{\boldsymbol{\varepsilon}}(\mathbf{x}) = \int d^3x' K_h(\mathbf{x} - \mathbf{x}') \boldsymbol{\varepsilon}(\mathbf{x}'). \quad (2)$$

Here  $K_h(\mathbf{x} - \mathbf{x}')$  is an isotropic, scalar kernel that depends only on the distance  $|\mathbf{x} - \mathbf{x}'|$  between two points  $\mathbf{x}, \mathbf{x}'$  in space. For concreteness, we use a normalized Gaussian kernel  $K_h(\mathbf{x}) = (4\pi h^2)^{-3/2} e^{-|\mathbf{x}|^2/(4h^2)}$ , with  $h$  being a suitable mesoscopic length scale that controls the amount of coarse-graining. Nonetheless, as we demonstrate in the Supplemental Material (SM) [29], our results are independent of our choice for this kernel.

The stress  $\boldsymbol{\sigma}$  computed using Eq. (1) models the correct elastic response of the elastomer, while simultaneously allowing us to use the strain  $\boldsymbol{\varepsilon}$  to capture compositional changes at molecular length scales. This model is a particular instance of the Eringen framework [30–32] of nonlocal elasticity, and it leads to an elastic energy density  $w(\boldsymbol{\varepsilon})$  of the form

$$w(\boldsymbol{\varepsilon}) = \frac{\lambda}{2}(\text{tr } \boldsymbol{\varepsilon})(\text{tr } \bar{\boldsymbol{\varepsilon}}) + \mu \text{tr}(\boldsymbol{\varepsilon} \bar{\boldsymbol{\varepsilon}}), \quad (3)$$

obtained by contracting the strain  $\boldsymbol{\varepsilon}$  with the stress  $\boldsymbol{\sigma}$  in Eq. (1) expressed in terms of  $\bar{\boldsymbol{\varepsilon}}$ . As the kernel  $K_h$  is positive-definite and normalized,  $w(\boldsymbol{\varepsilon})$  remains positive, bounded from below, and reduces to the usual Hookean energy density in the limit  $h \rightarrow 0$ .

Let the elastomer be isotropically swollen initially at a temperature  $T$  with a constant volume fraction  $\phi_0$  of the polymer network. Compositional changes that occur as the temperature is lowered cause the local network volume fraction  $\phi(\mathbf{x})$  at a point  $\mathbf{x}$  to deviate from  $\phi_0$ . The grand-canonical free energy of the elastomer is then given by

$$\mathcal{F}[\psi, \boldsymbol{\varepsilon}] = \int d^3x \left[ f(\psi) + \frac{1}{2} \kappa |\nabla \psi|^2 + w(\boldsymbol{\varepsilon}) - \eta \psi \right]. \quad (4)$$

Here we have defined the order parameter (phase field)  $\psi(\mathbf{x}) = \phi(\mathbf{x}) - \phi_c$  assuming that the polymer-solvent system has a critical point  $(\phi_c, T_c)$ , and take the mixing free-energy density  $f(\psi)$  to be in a Landau form

$$f(\psi) = \frac{1}{2} a (T - T_c) \psi^2 + \frac{1}{4} b \psi^4, \quad (5)$$

with  $a$  and  $b$  being positive phenomenological constants. Also included in Eq. (4) is the elastic energy density  $w(\boldsymbol{\varepsilon})$  and a gradient-squared term with an interfacial parameter

$\kappa > 0$  to penalize spatial variations in  $\psi$ . Finally,  $\eta$  is a Lagrange multiplier to constrain the mean value of  $\psi$  to  $\psi_0 = \phi_0 - \phi_c$ , thereby conserving the total volume of the polymer network.

For small deformations of the elastomer close to the critical point, the strain  $\boldsymbol{\varepsilon}$  and the order parameter  $\psi$  are related by a material conservation relation (SM [29]),

$$\text{tr } \boldsymbol{\varepsilon} = \nabla \cdot \mathbf{u} \approx -\phi_c^{-1} \psi. \quad (6)$$

Compositional changes in the polymer volume fraction during temperature quenches arise primarily via solvent diffusion. This allows us to disregard shear deformations and use Eq. (6) to write the total elastic energy as a binary interaction in  $\psi$  mediated by the coarse-graining kernel  $K_h$ .

For linear stability analysis of Eq. (4), we express the order parameter  $\psi(\mathbf{x})$  and the kernel  $K_h(\mathbf{x})$  in terms of their Fourier transforms,  $\psi_{\mathbf{q}} = \int d^3x e^{-i\mathbf{q} \cdot \mathbf{x}} \psi(\mathbf{x})$  and  $K_h(\mathbf{q}) = e^{-h^2 q^2}$ . The total free energy in Fourier space then takes the form (SM [29])

$$\mathcal{F}[\psi] = \frac{1}{2} \int \frac{d^3q}{(2\pi)^3} \psi_{-\mathbf{q}} F_{\mathbf{q}} \psi_{\mathbf{q}} + \int d^3x \left( \frac{1}{4} b \psi^4 - \eta \psi \right), \quad (7)$$

where  $F_{\mathbf{q}}$  is the Fourier transform of the effective binary interaction for  $\psi$  given by

$$F_{\mathbf{q}} = a(T - T_c) + \kappa q^2 + M e^{-h^2 q^2}. \quad (8)$$

Here  $q = |\mathbf{q}|$  and  $M = (\lambda + 2\mu)/\phi_c^2$  is the rescaled longitudinal modulus [33, 34] of the swollen elastomer. Also, as we are limiting ourselves to linear analysis, we have left the nonquadratic terms of Eq. (7) untransformed.

The second term in Eq. (8), which favors long-range (small  $q$ ) modulations in  $\psi$ , measures the energy cost to create interfaces. Meanwhile, the elastic term  $M e^{-h^2 q^2}$  favors short-range (large  $q$ ) modulations. Hence, we expect the emergence of a stable, spatially modulated phase at an intermediate length scale, provided that the elastic term is adequately large. The characteristic size of the modulated phase scales as  $\Lambda \sim 2\pi q_m^{-1}$ , where  $q_m$  is the critical wavenumber at which  $F_{\mathbf{q}}$  acquires its minimum. From Eq. (8), we see that  $F_{\mathbf{q}}$  has a minimum at a nonzero  $q_m$  given by

$$q_m^2 = h^{-2} \ln \gamma, \quad (9)$$

only if the dimensionless parameter  $\gamma = M h^2 / \kappa > 1$ . The parameter  $\gamma$ , which measures the relative importance of elastic and interfacial effects, is analogous to the (inverse) elastocapillary number [20, 35]. If the elastic energy cost exceeds the cost to form interfaces ( $\gamma > 1$ ), the system can minimize its total energy by creating many stable, finite-sized domains, resulting in microphase separation.

During a temperature quench from the uniform phase with  $\psi(\mathbf{x}) = \psi_0$ , the onset of microphase separation is indicated by linear instability in the fluctuations. By setting  $\psi(\mathbf{x}) = \psi_0 + \delta\psi(\mathbf{x})$  and expanding Eq. (7) to

quadratic order in the fluctuations  $\delta\psi(\mathbf{x})$ , we find that such an instability occurs at a temperature where  $F_q = -3b\psi_0^2$  and  $q = q_m$ . This leads to an estimate for the temperature  $T_m$  at which microphase separation sets in, which we find to be

$$T_m(\psi_0) = T_c - a^{-1} [3b\psi_0^2 + M\gamma^{-1} (1 + \ln \gamma)]. \quad (10)$$

Because  $\gamma > 1$ , we see that  $T_m(\psi_0) < T_c$  for all  $\psi_0$ . Furthermore,  $T_m$  decreases linearly with the modulus  $M$ , showing that deeper temperature quenches are required to induce microphase separation in stiffer elastomers.

*Comparison to experiments.*— Apart from the intermolecular distance, a relevant length scale in swollen elastomers is the root-mean-square end-to-end distance  $\xi$  of the segments between adjacent cross-links in the polymer network [36–39] (Fig. 1). Taking each segment to be a freely-jointed chain with a Flory ratio  $C_\infty$  [40], composed of  $N$  repeat units of length  $\ell$ , we have  $\xi = \phi_c^{-1/3} (C_\infty N)^{1/2} \ell$  [40]. Here, the additional factor  $\phi_c^{-1/3}$  accounts for the stretch due to isotropic swelling. If the segments and the repeat units have molecular masses  $m_s$  and  $m_r$ , respectively, then  $N = m_s/m_r$ . Assuming that the elastomer has a mass density  $\rho$ , its Young’s modulus in the dry state is  $Y = 3\rho k_B T/m_s$  [41]. Using this expression to write  $m_s$  and  $N$  in terms of  $Y$ , we find that the end-to-end distance scales as [37, 38]

$$\xi \sim \phi_c^{-1/3} (3B/Y)^{1/2}, \quad (11)$$

where the material-dependent parameter  $B$  is given by

$$B = C_\infty \rho \ell^2 k_B T / m_r, \quad (12)$$

with  $k_B$  being the Boltzmann constant. See the SM [29] for further details. For the polydimethylsiloxane (PDMS) elastomers used in the experiments of Ref. [24], we find  $B = 0.024 \text{ kPa } \mu\text{m}^2$ , which gives  $\xi \sim 15\text{--}150 \text{ nm}$  for the experimental range of  $Y \sim 10\text{--}800 \text{ kPa}$ . Compared to  $\xi$ , the intermolecular length scale ( $\sim \ell$ ) is of the order of a few Å. The polymer network within the elastomer can be treated as an elastic continuum only at length scales larger than, but proportional to,  $\xi$ . For this reason, we take the coarse-graining length scale to be  $h = n\xi$ , with  $n$  being the average number of cross-links we coarse-grain over in each direction (Fig. 1).

In order to estimate the domain size  $\Lambda$  of the microphases, we note that the rescaled longitudinal modulus  $M$  of an elastomer is related to its dry Young’s modulus  $Y$  via  $M \sim \frac{1}{3} \phi_c^{-5/3} Y$  [29, 42]. Interface formation occurs at intermolecular length scales, so we estimate the interfacial parameter as  $\kappa \sim k_B T / \ell$  [43]. With the choice  $h = n\xi$ , the parameter  $\gamma$  is independent of  $Y$ , and using Eqs. (9) and (11) we find the scaling

$$\Lambda \sim 2\pi \left[ \frac{3Bn^2\phi_c^{-2/3}}{Y \ln \left( Bn^2\kappa^{-1}\phi_c^{-7/3} \right)} \right]^{1/2}. \quad (13)$$

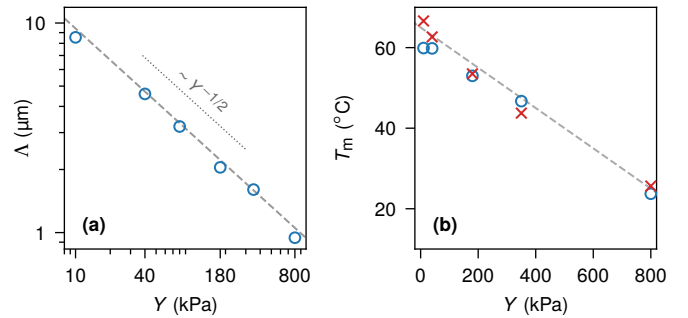


FIG. 2. (a) Domain size  $\Lambda$  as a function of the Young’s modulus  $Y$  of the dry elastomer (log-log plot). The circles indicate experimental values of  $\Lambda$  for PDMS elastomers from Ref. [24], showing the scaling  $\Lambda \sim Y^{-1/2}$ . The dashed line represents the prediction from Eq. (13) with  $\kappa = 0.013 \text{ kPa } \mu\text{m}^2$  and fitting parameters  $n = 35$ ,  $\phi_c = 0.2$ . (b) Decrease in the microphase separation temperature  $T_m$  with  $Y$ . The circles show the experimental values of  $T_m$  for an initial swelling temperature of  $60^\circ\text{C}$ . The crosses represent  $T_m$  estimated from Eq. (10) using experimental values of the mean polymer volume fraction  $\phi_0$ , with the dashed guideline illustrating the linearity between  $T_m$  and  $Y$ . Other fitting parameters are  $a = 0.025 \text{ kPa K}^{-1}$ ,  $b = 2 \text{ kPa}$ , and  $T_c = 70^\circ\text{C}$ .

In Fig. 2(a), we compare the experimental results and Eq. (13) and find good agreement between the two. Furthermore, as we see from Fig. 2(b), the microphase separation temperature  $T_m$  linearly decreases with  $Y$ , which is consistent with the prediction in Eq. (10). We show in the SM [29] that these scalings for  $\Lambda$  and  $T_m$  are agnostic to the choice of the kernel  $K_h$  in Eq. (2).

Close to the critical point, the domain boundaries of the microphases are diffuse (weak segregation), and they are well approximated as modulations in the order parameter  $\psi$  with a wavenumber  $q = q_m$  [44, 45]. A phase diagram in the  $(\phi_0, T)$  plane constructed using this one-mode approximation is presented in Fig. 3(a), with the analytical steps detailed in the SM [29]. For simplicity, we have only examined 2D modulations in the phase diagram. Nonetheless, it shows excellent agreement with the equilibrium phases found by numerically minimizing the free energy in 3D [Figs. 3(b) and 3(c)]. Near the critical point, there are three distinct phases: a uniform phase, a droplet (hexagonal) phase consisting of solvent-rich droplets embedded within the elastomer, and a stripe phase composed of alternating solvent-rich and solvent-deficient layers. An “inverted” droplet phase also appears at low  $\phi_0$ . The phase diagram has the same topology as phase diagrams for other modulated systems [46–49] and, in principle, there should be regions of phase coexistence. However, for the experimental parameter ranges used here, the widths of these regions are very small, and therefore are not depicted.

The phase diagram in Fig. 3 also shows good agreement with the experimental results and predicts the onset of microphase separation well. Experimentally, droplets are

seen in soft elastomers with  $Y \lesssim 40$  kPa. Only bicontinuous structures (different from stripes and droplets) are observed in stiff elastomers. However, because of the generic topology of the theoretical phase diagram, irrespective of the stiffness, we expect the droplet phase to always appear first during an off-critical temperature quench. This suggests that some other mechanism is responsible for the emergence of the bicontinuous structures in stiffer samples, e.g., shear deformations or nonlinear effects, which we have neglected.

*Summary and outlook.*— Using a phase-field model for swollen elastomers, we have predicted the possibility of a microphase separation arising from an imbalance between the intermolecular length scale and the mesoscopic coarseness of network elasticity. The elastomer remains stable with an intrinsically selected length scale if the free-energy contribution from the network elasticity is adequately large compared to the interfacial energy costs. Our scaling predictions for the domain size and the microphase separation temperature as a function of the elastic moduli are consistent with recent experimental observations [24].

In a recent theoretical work [50] inspired by the same experiments, a 1D nonlocal model was used to derive the scaling  $\Lambda \sim Y^{-1/2} h^{1/2} \kappa^{1/4}$  in the strong-segregation limit, taking the nonlocality scale  $h$  and the Young’s modulus  $Y$  to be independent. This scaling is different from our 3D result in Eq. (13) for weak segregation, which also takes into account the inter-dependence of  $h$  and  $Y$ . Extensions of our theory to ternary systems in the strong segregation regime could help elucidate the non-power-law scaling of the domain size observed in earlier experiments [12]. Our framework can also be used to study other systems where elasticity and thermodynamics often operate at different length scales, such as certain porous materials [51, 52], metals [2, 53], colloidal suspensions [54], etc.

We thank Ram Adar, Amit Kumar, and Sam Safran for useful conversations. M.M. acknowledges partial support through the Bloomfield Fellows Program at Tel Aviv University. H.D. thanks Lev Truskinovsky for helpful discussions and acknowledges support from the Israel Science Foundation (ISF Grant No. 1611/24). D.A. acknowledges support from the Israel Science Foundation (ISF Grant No. 226/24).

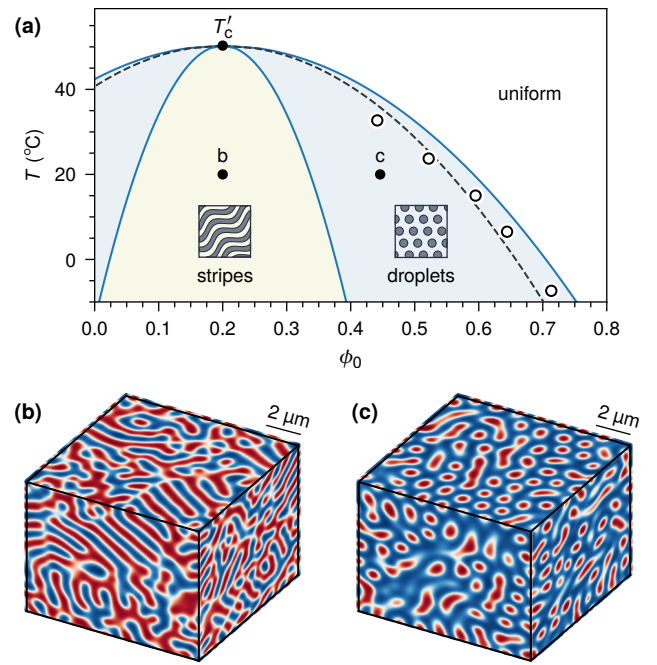


FIG. 3. (a) Phase diagram in the  $(\phi_0, T)$  plane for an elastomer with a dry Young’s modulus  $Y = 800$  kPa. Here  $T$  is the temperature, and  $\phi_0$  is the mean polymer volume fraction. Other parameters are the same as in Fig. 2. The solid curves show the phase boundaries (binodals). Phase coexistence regions are not depicted as they are very narrow. The dashed curve depicts the microphase separation temperature  $T_m$  from Eq. (10) with a shifted critical temperature  $T_c' = T_m(0)$ . The open circles represent experimental results from Ref. [24]. (b), (c) Equilibrium morphologies of the elastomer obtained by numerically minimizing the free energy, Eq. (7), with the corresponding  $(\phi_0, T)$  values marked in (a). Solvent-rich (small  $\phi_0$ ) and solvent-deficient (large  $\phi_0$ ) regions are highlighted in red and blue, respectively.

[1] J. W. Cahn, On spinodal decomposition, *Acta Metall.* **9**, 795 (1961).  
[2] P. Fratzl, O. Penrose, and J. L. Lebowitz, Modeling of phase separation in alloys with coherent elastic misfit, *J. Stat. Phys.* **95**, 1429 (1999).  
[3] Y. Rabin and S. Panyukov, Scattering profiles of charged gels: Frozen inhomogeneities, thermal fluctuations, and microphase separation, *Macromolecules* **30**, 301 (1997).  
[4] O. Peleg, M. Kröger, I. Hecht, and Y. Rabin, Filamentous networks in phase-separating two-dimensional gels, *EPL* **77**, 58007 (2007).

[5] J. Dervaux and M. B. Amar, Mechanical instabilities of gels, *Annu. Rev. Condens. Matter Phys.* **3**, 311–332 (2012).  
[6] J.-C. Loudet, P. Barois, and P. Poulin, Colloidal ordering from phase separation in a liquid-crystalline continuous phase, *Nature* **407**, 611–613 (2000).  
[7] J.-M. Choi, A. S. Holehouse, and R. V. Pappu, Physical principles underlying the complex biology of intracellular phase transitions, *Annu. Rev. Biophys.* **49**, 107 (2020).  
[8] H. Tanaka, Viscoelastic phase separation in biological cells, *Commun. Phys.* **5**, 167 (2022).  
[9] D. S. W. Lee, A. R. Strom, and C. P. Brangwynne, The mechanobiology of nuclear phase separation, *APL Bioeng.* **6**, 021503 (2022).  
[10] A. Kumar and S. A. Safran, Fluctuations and shape dependence of microphase separation in systems with long-range interactions, *Phys. Rev. Lett.* **131**, 258401 (2023).  
[11] D. Deviri and S. A. Safran, Mechanosensitivity of phase separation in an elastic gel, *Eur. Phys. J. E* **47**, 16 (2024).  
[12] R. W. Style, T. Sai, N. Fanelli, M. Ijavi, K. Smith-



- Mannschott, Q. Xu, L. A. Wilen, and E. R. Dufresne, Liquid-liquid phase separation in an elastic network, *Phys. Rev. X* **8**, 011028 (2018).
- [13] K. A. Rosowski, T. Sai, E. Vidal-Henriquez, D. Zwicker, R. W. Style, and E. R. Dufresne, Elastic ripening and inhibition of liquid-liquid phase separation, *Nat. Phys.* **16**, 422 (2020).
- [14] K. A. Rosowski, E. Vidal-Henriquez, D. Zwicker, R. W. Style, and E. R. Dufresne, Elastic stresses reverse ostwald ripening, *Soft Matter* **16**, 5892 (2020).
- [15] S. Wilken, A. Chaderjian, and O. A. Saleh, Spatial organization of phase-separated DNA droplets, *Phys. Rev. X* **13**, 031014 (2023).
- [16] J. X. Liu, M. P. Haataja, A. Košmrlj, S. S. Datta, C. B. Arnold, and R. D. Priestley, Liquid-liquid phase separation within fibrillar networks, *Nat. Commun.* **14**, 6085 (2023).
- [17] X. Ren and L. Truskinovsky, Finite scale microstructures in nonlocal elasticity, *J. Elast.* **59**, 319–355 (2000).
- [18] M. Kothari and T. Cohen, Effect of elasticity on phase separation in heterogeneous systems, *J. Mech. Phys. Solids* **145**, 104153 (2020).
- [19] X. Wei, J. Zhou, Y. Wang, and F. Meng, Modeling elastically mediated liquid-liquid phase separation, *Phys. Rev. Lett.* **125**, 268001 (2020).
- [20] P. Ronceray, S. Mao, A. Košmrlj, and M. P. Haataja, Liquid demixing in elastic networks: Cavitation, permeation, or size selection?, *EPL* **137**, 67001 (2022).
- [21] S. Biswas, B. Mukherjee, and B. Chakrabarti, Thermodynamics predicts a stable microdroplet phase in polymer-gel mixtures undergoing elastic phase separation, *Soft Matter* **18**, 8117 (2022).
- [22] J. Little, A. J. Levine, A. R. Singh, and R. Bruinsma, Finite-strain elasticity theory and liquid-liquid phase separation in compressible gels, *Phys. Rev. E* **107**, 024418 (2023).
- [23] Y. Grabovsky and L. Truskinovsky, A class of nonlinear elasticity problems with no local but many global minimizers, *J. Elast.* **154**, 147–171 (2023).
- [24] C. Fernández-Rico, S. Schreiber, H. Oudich, C. Lorenz, A. Sicher, T. Sai, V. Bauernfeind, S. Heyden, P. Carrara, L. D. Lorenzis, R. W. Style, and E. R. Dufresne, Elastic microphase separation produces robust bicontinuous materials, *Nat. Mater.* **23**, 124 (2024).
- [25] H. Nishimori and A. Onuki, Pattern formation in phase-separating alloys with cubic symmetry, *Phys. Rev. B* **42**, 980 (1990).
- [26] E. Vidal-Henriquez and D. Zwicker, Cavitation controls droplet sizes in elastic media, *Proc. Natl. Acad. Sci. U.S.A.* **118**, e2102014118 (2021).
- [27] M. S. Dimitriyev, Y.-W. Chang, P. M. Goldbart, and A. Fernández-Nieves, Swelling thermodynamics and phase transitions of polymer gels, *Nano Futures* **3**, 042001 (2019).
- [28] M. Doi, Gel dynamics, *J. Phys. Soc. Jpn.* **78**, 052001 (2009).
- [29] See the Supplemental Material, which includes Refs. [55–65], for further details on (i) the material conservation relation [Eq. (6)] and the free energy [Eq. (7)], (ii) comparison with experiments and derivations of Eqs. (11)–(13), (iii) phase diagram and Eq. (10), (iv) universality of the scaling results, and (v) numerical techniques.
- [30] A. Eringen, C. Speziale, and B. Kim, Crack-tip problem in non-local elasticity, *J. Mech. Phys. Solids* **25**, 339–355 (1977).
- [31] A. C. Eringen, Theory of nonlocal elasticity and some applications, *Res Mech.* **21**, 313 (1987).
- [32] C. Polizzotto, P. Fuschi, and A. Pisano, A strain-difference-based nonlocal elasticity model, *Int. J. Solids Struct.* **41**, 2383–2401 (2004).
- [33] Y. Rabin and A. Onuki, Osmotic and longitudinal moduli of polymer gels, *Macromolecules* **27**, 870 (1994).
- [34] J. F. Doyle, *Wave Propagation in Structures*, 3rd ed. (Springer, New York, NY, 2021).
- [35] Q. Liu, T. Ouchi, L. Jin, R. Hayward, and Z. Suo, Elastocapillary crease, *Phys. Rev. Lett.* **122**, 098003 (2019).
- [36] T. Canal and N. A. Peppas, Correlation between mesh size and equilibrium degree of swelling of polymeric networks, *J. Biomed. Mater. Res.* **23**, 1183 (1989).
- [37] S. H. Yoo, C. Cohen, and C.-Y. Hui, Mechanical and swelling properties of PDMS interpenetrating polymer networks, *Polymer* **47**, 6226–6235 (2006).
- [38] E. Parrish, M. A. Caporizzo, and R. J. Composto, Network confinement and heterogeneity slows nanoparticle diffusion in polymer gels, *J. Chem. Phys.* **146**, 203318 (2017).
- [39] N. R. Richbourg and N. A. Peppas, The swollen polymer network hypothesis: Quantitative models of hydrogel swelling, stiffness, and solute transport, *Prog. Polym. Sci.* **105**, 101243 (2020).
- [40] M. Rubinstein and R. H. Colby, *Polymer Physics* (Oxford University Press, Oxford, 2003).
- [41] T. P. Lodge and P. C. Hiemenz, *Polymer Chemistry*, 3rd ed. (CRC Press, Boca Raton, FL, 2020).
- [42] A. Onuki, Theory of phase transition in polymer gels, in *Responsive Gels: Volume Transitions I*, edited by K. Dušek (Springer, Berlin, 1993) pp. 63–121.
- [43] S. Leibler and D. Andelman, Ordered and curved mesostructures in membranes and amphiphilic films, *J. Phys. France* **48**, 2013–2018 (1987).
- [44] M. Seul and D. Andelman, Domain shapes and patterns: The phenomenology of modulated phases, *Science* **267**, 476 (1995).
- [45] D. Andelman and R. E. Rosensweig, Modulated phases: Review and recent results, *J. Phys. Chem. B* **113**, 3785 (2009).
- [46] T. Garel and S. Doniach, Phase transitions with spontaneous modulation—the dipolar Ising ferromagnet, *Phys. Rev. B* **26**, 325 (1982).
- [47] D. Andelman, F. Brogård, and J.-F. Joanny, Phase transitions in Langmuir monolayers of polar molecules, *J. Chem. Phys.* **86**, 3673 (1987).
- [48] K. R. Elder and M. Grant, Modeling elastic and plastic deformations in nonequilibrium processing using phase field crystals, *Phys. Rev. E* **70**, 051605 (2004).
- [49] N. Provatas and K. Elder, *Phase-Field Methods in Materials Science and Engineering* (Wiley-VCH, Weinheim, 2011).
- [50] Y. Qiang, C. Luo, and D. Zwicker, Nonlocal elasticity yields equilibrium patterns in phase separating systems, *Phys. Rev. X* **14**, 021009 (2024).
- [51] O. Coussy, *Poromechanics* (John Wiley & Sons, New York, NY, 2004).
- [52] O. W. Paulin, L. C. Morrow, M. G. Hennessy, and C. W. MacMinn, Fluid–fluid phase separation in a soft porous medium, *J. Mech. Phys. Solids* **164**, 104892 (2022).
- [53] A. Onuki, Long-range interactions through elastic fields in phase-separating solids, *J. Phys. Soc. Jpn.* **58**, 3069 (1977).

- (1989).
- [54] H. Tanaka, Y. Nishikawa, and T. Koyama, Network-forming phase separation of colloidal suspensions, *J. Phys.: Condens. Matter* **17**, L143 (2005).
  - [55] O. Gonzalez and A. M. Stuart, *A First Course in Continuum Mechanics* (Cambridge University Press, New York, NY, 2008).
  - [56] J. E. Mark, Some interesting things about polysiloxanes, *Acc. Chem. Res.* **37**, 946–953 (2004).
  - [57] A. Onuki, Theory of pattern formation in gels: Surface folding in highly compressible elastic bodies, *Phys. Rev. A* **39**, 5932 (1989).
  - [58] D. Jia and M. Muthukumar, Theory of charged gels: Swelling, elasticity, and dynamics, *Gels* **7**, 49 (2021).
  - [59] S. D. Reinitz, E. M. Carlson, R. A. Levine, K. J. Franklin, and D. W. Van Citters, Dynamical mechanical analysis as an assay of cross-link density of orthopaedic ultra high molecular weight polyethylene, *Polymer Testing* **45**, 174 (2015).
  - [60] J. M. Aguirregabiria, A. Hernández, and M. Rivas,  $\delta$ -function converging sequences, *Am. J. Phys.* **70**, 180 (2002).
  - [61] A. Bray, Theory of phase-ordering kinetics, *Adv. Phys.* **43**, 357 (1994).
  - [62] D. J. Eyre, *An Unconditionally Stable One-Step Scheme for Gradient Systems*, Tech. Rep. (University of Utah, 1998).
  - [63] B. P. Vollmayr-Lee and A. D. Rutenberg, Fast and accurate coarsening simulation with an unconditionally stable time step, *Phys. Rev. E* **68**, 066703 (2003).
  - [64] S. Yoon, D. Jeong, C. Lee, H. Kim, S. Kim, H. G. Lee, and J. Kim, Fourier-spectral method for the phase-field equations, *Mathematics* **8**, 1385 (2020).
  - [65] <https://github.com/manu-mannattil/elastomer>.

# Supplemental Material: Theory of Microphase Separation in Elastomers

Manu Mannattil,<sup>1,2</sup> Haim Diamant,<sup>2</sup> David Andelman<sup>2</sup>

<sup>1</sup>*School of Chemistry, Tel Aviv University, Ramat Aviv, Tel Aviv 69978, Israel*

<sup>2</sup>*School of Physics and Astronomy, Tel Aviv University, Ramat Aviv, Tel Aviv 69978, Israel*

This Supplemental Material is organized as follows: In Sec. I, we derive an expression for the free energy of swollen elastomers. A comparison of recent experimental results with our model is presented in Sec. II, with phase diagrams discussed in Sec. III. In Sec. IV, we describe a general coarse-graining procedure and prove that the domain size scaling is independent of the specific choice of the coarse-graining kernel. Finally, in Sec. V, we discuss the numerical techniques used in this work.

## I. FREE ENERGY OF SWOLLEN ELASTOMERS

### A. Elastic deformation and material conservation

Consider an isotropically swollen elastomer with a constant polymer network volume fraction  $\phi_0$  occupying a finite volume in 3D and described by the Lagrangian (material) coordinates  $\mathbf{x}$ . As the elastomer gets deformed, the coordinate  $\mathbf{x}$  gets transformed to the Eulerian (spatial) coordinate  $\mathbf{y}$ , and the local polymer volume fraction changes from  $\phi_0$  to  $\phi(\mathbf{y})$ . We assume that the deformation is captured by a smooth invertible map  $\chi$  as

$$\mathbf{y} = \chi(\mathbf{x}) = \mathbf{x} + \mathbf{u}(\mathbf{x}), \quad (\text{S1})$$

where we have introduced the displacement field  $\mathbf{u}(\mathbf{x})$ . Material conservation within an arbitrary subvolume  $\Sigma$  before and after deformation gives [55]

$$\int_{\Sigma} d^3x \phi_0 = \int_{\chi(\Sigma)} d^3y \phi(\mathbf{y}) = \int_{\Sigma} d^3x |\det \nabla \chi| \phi(\mathbf{x}). \quad (\text{S2})$$

In the last step in Eq. (S2), we have changed variables back to  $\mathbf{x}$  and write  $\phi(\chi(\mathbf{x}))$  as just  $\phi(\mathbf{x})$  for simplicity. This introduces the Jacobian factor  $\det(\nabla \chi)$ , which is always positive as physical deformations preserve orientation. Because of the arbitrariness of  $\Sigma$ , we equate the first and last integrands in Eq. (S2) to obtain the local material conservation relation

$$\begin{aligned} \phi_0 &= \phi(\mathbf{x}) \det(\nabla \chi) = \phi(\mathbf{x}) \det(\mathbb{1} + \nabla \mathbf{u}) \\ &= \phi(\mathbf{x}) \left[ 1 + \nabla \cdot \mathbf{u} + \mathcal{O}(|\mathbf{u}|^2) \right]. \end{aligned} \quad (\text{S3})$$

For small deformations close to the critical point, we can expand both  $\phi_0$  and  $\phi(\mathbf{x})$  around  $\phi = \phi_c$  and express  $\nabla \cdot \mathbf{u}$  as

$$\nabla \cdot \mathbf{u} = -\phi_c^{-1} \psi + \mathcal{O}(\psi_0) + \mathcal{O}(\psi^2). \quad (\text{S4})$$

Here  $\psi_0 = \phi_0 - \phi_c$  and  $\psi(\mathbf{x}) = \phi(\mathbf{x}) - \phi_c$ . This completes the derivation of Eq. (6) of the Letter.

### B. Energy of a swollen elastomer under small deformations

The Fourier transforms of the strain  $\boldsymbol{\varepsilon}$  and the coarse-grained strain  $\bar{\boldsymbol{\varepsilon}}$  are

$$\varepsilon_{jk}(\mathbf{q}) = \frac{i}{2} [q_j u_k(\mathbf{q}) + q_k u_j(\mathbf{q})] \quad \text{and} \quad \bar{\varepsilon}_{jk}(\mathbf{q}) = \frac{i}{2} [q_j u_k(\mathbf{q}) + q_k u_j(\mathbf{q})] K_h(\mathbf{q}), \quad (\text{S5})$$

where  $\mathbf{u}_{\mathbf{q}} = \int d^3x e^{-i\mathbf{q}\cdot\mathbf{x}} \mathbf{u}(\mathbf{x})$  and  $K_h(\mathbf{q})$  are the Fourier transforms of the displacement field  $\mathbf{u}(\mathbf{x})$  and the coarse-graining kernel  $K_h(\mathbf{x})$ , respectively.<sup>1</sup> Making use of the Parseval–Plancherel identity, we find the elastic energy  $\mathcal{F}_{\text{el}}$  in Fourier space to be

$$\mathcal{F}_{\text{el}}[\mathbf{u}_{\mathbf{q}}] = \frac{1}{2} \int \frac{d^3q}{(2\pi)^3} K_h(\mathbf{q}) \left[ (2\mu + \lambda)(\mathbf{q} \cdot \mathbf{u}_{\mathbf{q}})(\mathbf{q} \cdot \mathbf{u}_{-\mathbf{q}}) + \mu q^2 \mathbf{u}_{\mathbf{q}}^{\perp} \cdot \mathbf{u}_{-\mathbf{q}}^{\perp} \right], \quad (\text{S6})$$

---

<sup>1</sup> For subscripted terms such as  $K_h(\mathbf{x})$ , we write the Fourier transform as  $K_h(\mathbf{q})$  to avoid ambiguity.

where  $\mathbf{u}_q^\perp = \mathbf{u}_q - q^{-2}(\mathbf{q} \cdot \mathbf{u}_q)\mathbf{q}$  is the transverse component of  $\mathbf{u}_q$ . After Fourier transforming the material conservation relation, Eq. (S4), which relates  $\mathbf{u}$  and  $\psi$ , we can write the elastic energy (up to additive constants) in Fourier space as

$$\mathcal{F}_{\text{el}}[\psi_{\mathbf{q}}, \mathbf{u}_{\mathbf{q}}^\perp] = \frac{1}{2}M \int \frac{d^3q}{(2\pi)^3} K_h(\mathbf{q})\psi_{\mathbf{q}}\psi_{-\mathbf{q}} + \frac{1}{2}\mu \int \frac{d^3q}{(2\pi)^3} q^2 K_h(\mathbf{q})\mathbf{u}_{\mathbf{q}}^\perp \cdot \mathbf{u}_{-\mathbf{q}}^\perp. \quad (\text{S7})$$

Here  $M = \phi_c^{-2}(\lambda + 2\mu)$  is the elastic part of the rescaled longitudinal (or the pressure-wave) modulus [33]. During phase separation, compositional changes in the polymer volume fraction arise primarily via solvent diffusion, which is not expected to affect the transverse shear modes  $\mathbf{u}^\perp$ . This allows us to discard them and write the total energy as

$$\begin{aligned} \mathcal{F}[\psi] &= \mathcal{F}_{\text{el}} + \int d^3x \left[ f(\psi) + \frac{1}{2}\kappa |\nabla\psi|^2 \right] \\ &= \frac{1}{2} \int \frac{d^3q}{(2\pi)^3} [a(T - T_c) + \kappa q^2 + MK_h(\mathbf{q})] \psi_{\mathbf{q}}\psi_{-\mathbf{q}} + \int d^3x \left( \frac{1}{4}b\psi^2 - \eta\psi \right). \end{aligned} \quad (\text{S8})$$

In the last step in Eq. (S8), we have written  $\mathcal{F}_{\text{el}}$  and the quadratic parts of both the mixing free energy  $f(\psi)$  and the interfacial energy  $\frac{1}{2}\kappa |\nabla\psi|^2$  in Fourier space. For a Gaussian kernel  $K_h(\mathbf{x}) = (4\pi h^2)^{-3/2}e^{-|\mathbf{x}|^2/(4h^2)}$  we have  $K_h(\mathbf{q}) = e^{-h^2q^2}$ . From the above equation, we deduce that the Fourier transform of the effective binary interaction for the  $\psi$  field is

$$F_{\mathbf{q}} = a(T - T_c) + \kappa q^2 + Me^{-h^2q^2}, \quad (\text{S9})$$

which completes the derivation of Eq. (7) of the Letter.

For computational purposes, it is also useful to consider the real-space representation of Eq. (S8), given by

$$\mathcal{F}[\psi] = \int d^3x \left[ \frac{1}{2}a(T - T_c)\psi^2 + \frac{1}{4}b\psi^4 + \frac{1}{2}\kappa |\nabla\psi|^2 + M\psi\bar{\psi} - \eta\psi \right], \quad (\text{S10})$$

where  $\bar{\psi}$  is the coarse-grained  $\psi$  field, defined using Eq. (2) as

$$\bar{\psi}(\mathbf{x}) = \int d^3x' K_h(\mathbf{x} - \mathbf{x}')\psi(\mathbf{x}'). \quad (\text{S11})$$

## II. COMPARISON WITH EXPERIMENTS

The experimental results in Ref. [24] are discussed in terms of the mass fraction  $c_{\text{oil}}$  of the oil (solvent) present in the elastomer. Assuming that the mass densities of the elastomer and the oil ( $\rho$  and  $\rho_{\text{oil}}$ , respectively) do not change considerably during the swelling process, the network volume fraction  $\phi$  is estimated from  $c_{\text{oil}}$  using

$$\phi = \frac{(1 - c_{\text{oil}})\rho_{\text{oil}}}{(1 - c_{\text{oil}})\rho_{\text{oil}} + c_{\text{oil}}\rho}. \quad (\text{S12})$$

The amount of oil absorbed depends on the dry Young's modulus of the elastomer  $Y$  and the temperature  $T$ . Because of this, the mass fraction  $c_{\text{oil}}$  varies between  $c_{\text{oil}} \approx 0.35$  ( $Y = 800$  kPa,  $T = 23$  °C) and  $c_{\text{oil}} \approx 0.80$  ( $Y = 10$  kPa,  $T = 80$  °C). Using the density values listed in Table I, which also lists other physical parameters, gives us a  $\phi$  roughly in the range 0.2–0.7.

An elastomer consists of many polymer chains cross-linked to form a polymer network, with the chains customarily assumed to follow Gaussian statistics. The elastic moduli of a swollen elastomer depends on the polymer network volume fraction  $\phi$ . However, the dependence is usually weak, and given that the elastomer is close to the critical point, we take  $\phi \approx \phi_c$  for simplicity in the estimates below. Assuming that the elastomer swells isotropically from a dry state composed entirely of the polymer network, its Lamé parameters<sup>2</sup>  $\lambda$  and  $\mu$  are [42, 58]

$$\lambda = \nu k_{\text{B}}T \left( \frac{1}{2}\phi_c - \phi_c^{1/3} \right) \quad \text{and} \quad \mu = \nu k_{\text{B}}T \phi_c^{1/3}. \quad (\text{S13})$$

Above,  $\nu$  is the strand density, defined as the average number of *strands* per unit volume. A strand is a segment of the polymer network between two adjacent cross-links, with no intervening cross-links in between [41]. The strand

<sup>2</sup> The Lamé parameter  $\lambda$  being negative in Eq. (S13) is not a cause for concern because the overall stability of an elastomer is determined by both thermodynamic and elastic contributions to the free energy. Indeed, this is why it is sometimes customary to work with osmotic moduli [28, 42, 57, 58], which take into account both contributions.



TABLE I. Physical and model parameters.

Parameter	Description	Value
$k_{\text{B}}T$	Thermal energy at $T = 300$ K	$4.14 \times 10^{-21}$ J
$m_{\text{r}}$	Molecular mass of PDMS repeat unit $[-\text{Si}(\text{CH}_3)_2\text{O}-]$	$1.23 \times 10^{-25}$ kg ( $74.2$ g mol $^{-1}$ )
$\ell$	Length of the PDMS repeat unit [56]	$3.28$ Å
$\rho$	Mass density of PDMS <sup>a</sup>	$970$ kg m $^{-3}$
$\rho_{\text{oil}}$	Mass density of the solvent (heptafluorobutyl methacrylate <sup>b</sup> )	$1345$ kg m $^{-3}$
$C_{\infty}$	Flory characteristic ratio for PDMS [40]	$6.8$
$\kappa$	Interfacial parameter ( $\sim k_{\text{B}}T/\ell$ [43])	$0.013$ kPa $\mu\text{m}^2$ ( $1.3 \times 10^{-11}$ J m $^{-1}$ )
$B$	$C_{\infty}\rho\ell^2k_{\text{B}}T/m_{\text{r}}$ [see Eq. (S17)]	$0.024$ kPa $\mu\text{m}^2$ ( $2.4 \times 10^{-11}$ J m $^{-1}$ )

<sup>a</sup> Vinyl terminated polydimethylsiloxane (DMS-V31) safety data sheet (Gelest, Morrisville, PA, 2014).

<sup>b</sup> 2,2,3,3,4,4,4-Heptafluorobutyl methacrylate (PC11102) safety data sheet (Apollo Scientific, Bredbury, UK, 2023).

density  $\nu$  is usually expressed in terms of the average molecular mass  $m_{\text{s}}$  of the strands and the dry mass density of the elastomer  $\rho$  as  $\nu = \rho/m_{\text{s}}$  [36, 41].

Although our discussion so far has been on the elastic moduli of the swollen elastomer, the results reported in Ref. [24] are in terms of the Young's modulus  $Y$  of the dry (i.e., unswollen) elastomer. For a dry elastomer,  $Y$  is given by [41]

$$Y = 3\nu k_{\text{B}}T = 3 \left( \frac{\rho}{m_{\text{s}}} \right) k_{\text{B}}T. \quad (\text{S14})$$

The above equation is frequently used to experimentally estimate  $m_{\text{s}}$  by measuring  $Y$ , e.g., via dynamic mechanical analysis [59].

For swollen elastomers, it is customary to use the end-to-end distance of the strand as the characteristic size of the network [38, 39]. Assuming that the strands behave like a freely-jointed chain modified by a Flory characteristic ratio  $C_{\infty}$ , the root-mean-square end-to-end distance  $\langle r^2 \rangle^{1/2}$  before swelling is given by the usual expression [41]

$$\langle r^2 \rangle^{1/2} = (C_{\infty}N)^{1/2}\ell. \quad (\text{S15})$$

Here,  $N$  is the degree of polymerization, i.e., the number of repeat units in the strand, and  $\ell$  is the length of the PDMS repeat unit  $[-\text{Si}(\text{CH}_3)_2\text{O}-]$ , taken to be twice the Si–O bond length of  $1.64$  Å [56] in siloxane backbones. For strands of molecular mass  $m_{\text{s}}$ , consisting of repeat units of mass  $m_{\text{r}}$ , the degree of polymerization is usually estimated as  $N = m_{\text{s}}/m_{\text{r}}$  [41]. Upon using Eq. (S14) to eliminate the strand mass  $m_{\text{s}}$  and express  $N$  in terms of the Young's modulus  $Y$  of the dry elastomer, one finds

$$N = \frac{m_{\text{s}}}{m_{\text{r}}} = \frac{3\rho k_{\text{B}}T}{Y m_{\text{r}}}. \quad (\text{S16})$$

Using the above equation, we see that for the PDMS elastomer used in the experiments,  $N$  ranges from about  $10^2$  (at  $Y = 800$  kPa) to about  $10^4$  (at  $Y = 10$  kPa). As the elastomer is assumed to swell from a completely dry state, the distance between the cross-links *increases* roughly by a factor of  $\phi_{\text{c}}^{-1/3}$  once it is swollen (assuming isotropy). Thus, the end-to-end distance  $\xi$  between the cross-links of a swollen elastomer scales as [37, 38]

$$\xi = \langle r^2 \rangle^{1/2} \phi_{\text{c}}^{-1/3} = \phi_{\text{c}}^{-1/3} \left( \frac{3B}{Y} \right)^{1/2} \quad \text{with} \quad B = C_{\infty}\rho\ell^2k_{\text{B}}T/m_{\text{r}}. \quad (\text{S17})$$

The parameter  $B$  has dimensions of energy per unit length, and we estimate it to be  $B = 0.024$  kPa  $\mu\text{m}^2$  (Table I). The dependence of  $\xi$  on  $\phi_{\text{c}}$  is weak for its expected range of  $\phi_{\text{c}} \sim 0.2$ – $0.7$ , and the above equation predicts a  $\xi$  between  $15$  nm (at  $Y = 800$  kPa) and  $150$  nm (at  $Y = 10$  kPa).

To estimate the microphase domain size, apart from  $\xi$ , we also require the rescaled longitudinal modulus  $M$  of the swollen elastomer. Using Eqs. (S13) and (S14), we express  $M$  in terms of the dry Young's modulus as

$$M = \phi_{\text{c}}^{-2}(\lambda + 2\mu) = \phi_{\text{c}}^{-2} \left( \frac{1}{6}\phi_{\text{c}} + \frac{1}{3}\phi_{\text{c}}^{1/3} \right) Y \sim \frac{1}{3}\phi_{\text{c}}^{-5/3}Y. \quad (\text{S18})$$

As we have remarked in the Letter, the coarse-graining length scale is  $h = n\xi$ , with  $n$  being the average number of cross-links over which we coarse-grain in each direction. Using Eqs. (S17) and (S18) we find the dimensionless parameter  $\gamma$  to be

$$\gamma = Mh^2\kappa^{-1} = Bn^2\kappa^{-1}\phi_c^{-7/3}. \quad (\text{S19})$$

Note that  $\gamma$  is independent of the Young's modulus  $Y$ , and it satisfies the condition  $\gamma > 1$  for the parameter values in Table I (even when  $n = 1$ ). We now see that the domain size  $\Lambda$  scales as

$$\Lambda \sim 2\pi q_m^{-1} = 2\pi h(\ln \gamma)^{-1/2} = 2\pi \left[ \frac{3Bn^2\phi_c^{-2/3}}{Y \ln(Bn^2\kappa^{-1}\phi_c^{-7/3})} \right]^{1/2}. \quad (\text{S20})$$

This completes the derivation of Eq. (13) of the Letter.

### III. PHASE DIAGRAM

We can use the one-mode approximation to analytically construct the phase diagram in the weak-segregation limit. Although the free energy in Eq. (7) of the Letter is defined over 3D space, we restrict ourselves to an analysis of 2D modulations for simplicity. In 2D, one typically considers two modulated phases: the stripe and droplet (hexagonal) phases and the uniform phase, devoid of modulations. Once the free energy for each of these phases is determined, the phase diagram can be determined via Maxwell construction. For brevity in presenting the results below, we define a dimensionless parameter

$$\Gamma = b^{-1} [a(T - T_c) + 3b\psi_0^2 + M\gamma^{-1}(1 + \ln \gamma)]. \quad (\text{S21})$$

*Uniform phase.* The uniform phase has a free energy density

$$f_U = \frac{1}{2} [a(T - T_c) + M] \psi_0^2 + \frac{1}{4} b\psi_0^4. \quad (\text{S22})$$

*Stripe phase.* For the stripe phase, we consider the stripe solution  $\psi_S = \psi_0 + A \cos(qx)$ , with  $A \cos(qx)$  representing a modulation of amplitude  $A$  and wavenumber  $q$  directed along one of the spatial directions. We substitute this solution in Eq. (S10) and minimize the free energy with respect to  $q$  and  $A$  to obtain the free-energy density  $f_S$  of the stripe phase as

$$f_S = f_U - \frac{b}{6}\Gamma^2, \quad \text{with} \quad q_m^2 = h^{-2} \ln \gamma \quad \text{and} \quad A^2 = -\frac{4}{3}\Gamma. \quad (\text{S23})$$

As the modulation amplitude must be real for the stripe solution to exist, setting  $\Gamma = 0$  in Eq. (S21) gives an estimate for the microphase separation temperature  $T_m$ , which we find to be

$$T_m = T_c - a^{-1} [3b\psi_0^2 + M\gamma^{-1}(1 + \ln \gamma)]. \quad (\text{S24})$$

The same expression for  $T_m$  can also be derived by linear stability analysis of the fluctuations around the uniform phase, as in Eq. (10) of the Letter.

*Droplet phase.* For the droplet (hexagonal) phase, we consider the solution [48]

$$\psi_D = \psi_0 + A \left[ \cos(qx) \cos(qy/\sqrt{3}) - \frac{1}{2} \cos(2qy/\sqrt{3}) \right]. \quad (\text{S25})$$

As with the stripe phase, we use this solution in Eq. (S10) and minimize the free energy with respect to  $q$  and  $A$  to find

$$q_m^2 = h^{-2} \ln \gamma \quad \text{and} \quad A_{\pm} = \frac{4}{5} \left[ \psi_0 \pm \frac{1}{3} (9\psi_0^2 - 15\Gamma)^{1/2} \right]. \quad (\text{S26})$$

The solution  $A_+$  corresponds to the droplet phase, and  $A_-$  corresponds to the ‘‘inverted’’ droplet phase, with the minimized free-energy density given by

$$f_D = f_U - \frac{3b}{64} A_{\pm}^2 (\psi_0 A_{\pm} - 2\Gamma). \quad (\text{S27})$$

We use Maxwell construction to equate each phase's chemical potential and osmotic pressure to find the coexistence curves between the different phases. This leads to the following set of equations, which, when solved numerically, gives the mean value of the order parameter in each of the phases:

$$\frac{\partial f_i}{\partial \psi_{0,i}} = \frac{\partial f_j}{\partial \psi_{0,j}} \quad \text{and} \quad \psi_{0,i} \left( \frac{\partial f_i}{\partial \psi_{0,i}} \right) - f_i = \psi_{0,j} \left( \frac{\partial f_j}{\partial \psi_{0,j}} \right) - f_j. \quad (\text{S28})$$

Above, the subscripts  $i, j$  refer to one of the three phases: U, S, or D.

#### IV. GENERAL COARSE-GRAINING PROCEDURE

We now describe a general procedure to construct a large class of useful coarse-graining kernels in 3D. Although the procedure is not the only method, many routinely used kernels can be constructed using this method.

Consider a general probability density function  $P(x)$  of a real random variable. Now, consider the family of densities  $P_h(x)$ , indexed by a parameter  $h > 0$ , and defined by

$$P_h(x) = h^{-1} P(h^{-1}x). \quad (\text{S29})$$

The density  $P_h(x)$  is also normalized, and it satisfies [60]

$$\lim_{h \rightarrow 0^+} P_h(x) = \delta(x), \quad (\text{S30})$$

where  $\delta(x)$  is the Dirac delta function. We additionally assume that  $P(x)$  has a well defined second moment  $\mu_2 = \int_0^\infty dx x^2 P(x)$  on the half-interval  $[0, \infty)$ . We can now use the density  $P_h(x)$  to define a spherically-symmetric convolution kernel  $K_h(\mathbf{x})$  in 3D as

$$K_h(\mathbf{x}) = (4\pi\mu_2h^2)^{-1} P_h(|\mathbf{x}|), \quad (\text{S31})$$

Using the 3D analogue of Eq. (S30), it can be shown that  $\lim_{h \rightarrow 0^+} K_h(\mathbf{x}) = \delta^3(\mathbf{x})$  [60] and we identify the parameter  $h$  with the coarse-graining length. For example, if we choose  $P(x)$  to be the Gaussian distribution  $P(x) = (4\pi)^{-1/2} e^{-x^2/4}$  with  $\mu_2 = 1$ , we have  $K_h(\mathbf{x}) = (4\pi h^2)^{-3/2} e^{-|\mathbf{x}|^2/(4h^2)}$  as in the Letter.

Because  $K_h(\mathbf{x})$  is spherically symmetric by construction, it is natural to compute its Fourier transform  $K_h(\mathbf{q})$  in spherical polar coordinates. Without loss of generality, we take the polar axis along  $\mathbf{q}$  so that  $\mathbf{q} \cdot \mathbf{r} = qr \cos \theta$ , where  $r$  is the radial coordinate and  $q = |\mathbf{q}|$ . After integrating over the polar angle  $\theta$  as well as the azimuthal angle, we find

$$\begin{aligned} K_h(\mathbf{q}) &= (\mu_2 h^2)^{-1} \int_0^\infty dr r^2 \text{sinc}(qr) P_h(r) \\ &= \mu_2^{-1} \int_0^\infty dr r^2 \text{sinc}(hqr) P(r) = K_1(hq), \end{aligned} \quad (\text{S32})$$

showing that  $K_h(\mathbf{q})$  is a function<sup>3</sup> of the product  $hq$ .

The Fourier transform of the effective binary interaction in Eq. (S8) is

$$F_{\mathbf{q}} = a(T - T_c) + \kappa q^2 + M K_h(\mathbf{q}). \quad (\text{S33})$$

The critical wavenumber  $q_m$  is where  $F_{\mathbf{q}}$  acquires its minimum. Using Eq. (S32), we find that  $q_m$  satisfies the equation

$$2\kappa q_m + M K_h'(q_m) = 2\kappa q_m + M h K_1'(hq_m) = 0. \quad (\text{S34})$$

Defining the parameter  $\gamma = M h^2 / \kappa$ , we can write the above equation as

$$2 + \gamma [(hq_m)^{-1} K_1'(hq_m)] = 0. \quad (\text{S35})$$

The coarse-graining length scale  $h \propto \xi \sim Y^{-1/2}$  using Eq. (S17) and the rescaled longitudinal modulus  $M \sim Y$  from Eq. (S18). Because of this, we see that the parameter  $\gamma$  is independent of both the Young's modulus  $Y$  and  $h$ , and Eq. (S35) would generally be a transcendental equation in the product  $hq_m$ . Any valid solution to this equation must

<sup>3</sup> For a general kernel  $K_h(\mathbf{x})$ , this can also be seen using dimensional arguments. As  $K_h(\mathbf{x})$  is normalized to unity, it must have dimensions of inverse volume, making its Fourier transform  $K_h(\mathbf{q})$  dimensionless. Because the wavenumber  $q$  has dimensions of inverse length, and  $h$  is the only other length scale that appears in its definition,  $K_h(\mathbf{q})$  can only be a function of  $hq$ .

always scale as  $q_m \sim h^{-1} \sim Y^{1/2}$  and the product  $hq_m$  would be a function of  $\gamma$  alone. Therefore, irrespective of the kernel  $K_h$ , we see that the domain size  $\Lambda$  follows the scaling

$$\Lambda \sim 2\pi q_m^{-1} \sim Y^{-1/2}. \quad (\text{S36})$$

The microphase separation temperature  $T_m$  is the temperature at which the fluctuations around the uniform state become linearly unstable. As this occurs when  $F_q = -3b\psi_0^2$  and  $q = q_m$ , using Eqs. (S32) and (S33), we find

$$T_m = T_c - a^{-1} [3b\psi_0^2 + \kappa q_m^2 + MK_1(hq_m)]. \quad (\text{S37})$$

Since the product  $hq_m$  is a function of  $\gamma$  alone, with  $q_m^2 \sim Y$  and  $M \sim Y$ , we see that  $T_m$  always decreases linearly with  $Y$ , independent of the kernel  $K_h$ .

## V. NUMERICAL TECHNIQUES

As the field  $\psi(\mathbf{x})$  is conserved (i.e., its spatial average is a constant), we can numerically minimize the free energy in Eq. (S10) by considering a “time”-dependent field<sup>4</sup>  $\psi(\mathbf{x}, t)$  and evolving it using Model B dynamics [49, 61]:

$$\frac{\partial \psi(\mathbf{x}, t)}{\partial t} = \nabla^2 \left( \frac{\delta \mathcal{F}}{\delta \psi} \right) = \nabla^2 [a(T - T_c)\psi(\mathbf{x}, t) + b\psi^3(\mathbf{x}, t) - \kappa \nabla^2 \psi(\mathbf{x}, t) + M\bar{\psi}(\mathbf{x}, t)]. \quad (\text{S38})$$

Here  $\nabla^2$  is the Laplacian,  $t$  is the time, and  $\bar{\psi}$  is the coarse-grained field defined in Eq. (S11). Time evolution is performed after Fourier transforming Eq. (S38) in space, which lets us compute spatial derivatives and convolutions efficiently using fast-Fourier techniques (assuming periodic boundary conditions). However, it is known that explicit first-order time stepping can lead to instabilities unless the time step  $\delta t$  is very small. Therefore, we use a semi-implicit method employing a linearly stabilized splitting scheme [62–64] to evolve the time-discretized version of Eq. (S38) in Fourier space, given by

$$\psi_{\mathbf{q}}(t + \delta t) = C_{\mathbf{q}}^{-1} \{A_{\mathbf{q}}\psi_{\mathbf{q}}(t) - B_{\mathbf{q}}[\psi^3(t)]_{\mathbf{q}}\}. \quad (\text{S39})$$

Here  $\psi_{\mathbf{q}}(t)$  and  $[\psi^3(t)]_{\mathbf{q}}$  are the Fourier transforms of  $\psi(\mathbf{x}, t)$  and  $\psi^3(\mathbf{x}, t)$ , respectively, and the coefficients  $A_{\mathbf{q}}$ ,  $B_{\mathbf{q}}$ , and  $C_{\mathbf{q}}$  are

$$A_{\mathbf{q}} = 1 - 3a(T - T_c)q^2 \delta t, \quad B_{\mathbf{q}} = bq^2 \delta t, \quad \text{and} \quad C_{\mathbf{q}} = 1 + [\kappa q^2 - 2a(T - T_c) + Me^{-h^2 q^2}] q^2 \delta t. \quad (\text{S40})$$

Although this method is only  $\mathcal{O}(\delta t)$  accurate in time, it is sufficient for our purposes of energy minimization. For the three-dimensional equilibrium configurations presented in Figs. 3(b) and 3(c) of the Letter, Eq. (S39) was evolved in a cubical domain of side length  $10 \mu\text{m}$  and  $256^3$  grid points for  $5 \times 10^3$  units of time with a time step of  $\delta t = 1$ . The initial field configurations  $\psi(\mathbf{x}, 0)$  were chosen randomly, and their spatial averages were set equal to  $\psi_0 = \phi_0 - \phi_c$ . All our numerical codes are publicly available [65].

---

<sup>4</sup> We use Eq. (S38) solely for the purposes for energy minimization. It will not describe the actual dynamical evolution of  $\psi$  seen in experiments, as it completely ignores the transport of material via hydrodynamic flow and related dissipative effects [28].